PCCP

PAPER

View Article Online
View Journal | View Issue

Cite this: *Phys. Chem. Chem. Phys.*, 2015, **17**, 16145

Enhanced photocurrent density of hematite thin films on FTO substrates: effect of post-annealing temperature†

Eun Soo Cho, Myung Jong Kang and Young Soo Kang*

Received 28th March 2015,
Accepted 20th May 2015

DOI: 10.1039/c5cp01823d

www.rsc.org/pccp

Fluorine doped tin oxide (FTO) is widely used as a substrate in the synthesis of a photo-reactive semiconductor electrode for solar water splitting. The hematite film on the surface of the FTO substrate annealed at 700 °C showed an enhanced photocurrent value with a maximum photocurrent of 0.39 mA cm^{-2} at 1.23 V *vs.* RHE under 1 sun illumination. This is a much enhanced photocurrent value of the hematite films than that of those annealed at temperatures lower than 700 °C. This is a promising approach for the enhancement of the photoelectrochemical properties of metal oxide thin films. This work reports on the mechanism of the annealing process of the synthesized hematite film to enhance the photocurrent value. Furthermore, this can be used for the enhanced efficiency of the solar water splitting reaction.

Introduction

Recently, due to energy crisis, developing a strategy for sustainable and environmentally friendly energy becomes an important part in chemistry research. Solar water splitting, producing oxygen and hydrogen gas from water upon illumination of sunlight, is a future promising technique for solar energy utilization. Photo-active semiconductors like TiO_2, ZnO, WO_3 and α-Fe_2O_3 are widely used photocatalyst materials for solar water splitting.[1–10] Among these candidate materials, hematite (α-Fe_2O_3) is an attractive photoanode material due to the several advantages such as a suitable band gap (~2.1 eV) for utilizing visible range solar light, high absorption ability of photons, good chemical stability under ambient conditions, abundant elements on the earth and low cost material for solar water splitting.[11,12]

There are several methods to synthesize hematite thin films including hydrothermal methods,[13–15] ALD methods,[16–19] atmospheric pressure chemical vapour deposition (APCVD) methods[20,21] and the deposition annealing (DA) method.[22] These methods involve a process of annealing at temperatures lower than 550 °C during the synthesis of hematite thin films on fluorine doped tin oxide (FTO) substrates. This is due to the thermal critical temperature for the durability of the fluorine doped tin oxide (FTO) substrate, which is used generally as a transparent and conductive oxide substrate for the synthesis of a hematite thin film.

In this research, the effect of annealing temperature on the photocurrent density of hematite films during the fabrication process by the DA method has been comparatively studied in the range of 550–800 °C. The highest photocurrent density was obtained by the annealing of a hematite film at 700 °C, of which temperature did not result in the distortion of the basic crystal structure of tin oxide in the FTO substrate. In the modified DA method, deposition of the precursor solution by spin coating and annealing was done to enhance the uniformity and reproducibility of the hematite thin film even with less thickness.

Experimental

Materials and synthesis

Iron(III) chloride hexahydrate ($FeCl_3 \cdot 6H_2O$, 98+%) used as a Fe precursor and absolute ethyl alcohol (C_2H_5OH, 99.9%) were obtained from Sigma Aldrich Chemical Co. and used as received without further purification. The washed FTO glass was treated by O_2 plasma. The 20 mM $FeCl_3$ ethanol solution was spin-coated on the FTO glass at 1200 rpm for 20 s. The spin-coated sample was dried and annealed at 300 °C in a hot plate for 5 min. This process is considered as one deposition and annealing (DA) cycle. The total number of DA cycles was varied from 10 to 40 in this work. To investigate the relation between the annealing temperature and photocurrent density of the hematite film on FTO, the samples were annealed for 3 h at various temperatures of 550 °C, 600 °C, 700 °C and 800 °C.

Korea Center for Artificial Photosynthesis and Department of Chemistry, Sogang University, Seoul 121-742, Korea. E-mail: yskang@sogang.ac.kr

† Electronic supplementary information (ESI) available: Additional detailed descriptions of sample images, TEM analysis, photoelectrochemical efficiencies, electro impedance spectroscopy (EIS), schematic drawings, XPS analysis, electron energy loss spectroscopy (EELS) analysis, and UV-vis photoelectron spectroscopy (UPS). See DOI: 10.1039/c5cp01823d

Characterization

The crystalline structure of the samples was investigated by using X-ray diffraction spectroscopy (XRD: Rigaku, Ultima 2000) with 0.5° min^{-1} scanning speed and in the range of 20°–80° with 2θ mode by using a radiation source of Cu Kα. Structural analysis has been carried out by transmission electron microscopy (TEM: JEOL, JEM-2100) using an energy dispersive spectroscopy (EDS) analysis system (Bruker Quantax 400) at an incident electron beam energy of 200 kV. The sample preparation for TEM analysis was performed by focused ion beam (FIB: Quanta 3D FEG). The surface image and morphology of samples were obtained by scanning electron microscopy (SEM: Hitachi, Horiba S-4300) operated at 20 KV of incident electron beam energy. Additionally, the surface image and roughness of samples were collected by atomic force microscopy (AFM: S.I.S. Surface Imaging Systems GmbH, Germany) in non-contact mode. The optical absorbance of the sample has been measured by UV-vis spectroscopy (UV-vis: Agilent, Cary 5000) with universal measurement accessory.

The photoelectrochemical (PEC) measurement system (Ivium, compactstat) was used to obtain the photocurrent density curves. The reaction area of the film is 0.64 cm^2 (the diameter is 0.90 cm.). Electrochemical impedance spectroscopy (EIS) curves were obtained to identify the impedance values of the hematite–electrolyte solution at room temperature. PEC measurement has been performed in an electrochemical system with three electrodes including a 3.0 M KCl saturated Ag/AgCl reference electrode and a platinum wire as the counter electrode with 1.0 M NaOH as the electrolyte.[23] The potential measured by the Ag/AgCl reference electrode can be converted into the reversible hydrogen electrode (RHE) using the following Nernst equation like;

$$E_{RHE} = E_{(Ag/AgCl)} + 0.059 \times pH + E^{0}_{(Ag/AgCl)}$$

where $E^{0}_{(Ag/AgCl)}$ is 0.1976 V at 25 °C, $E_{(Ag/AgCl)}$ is the experimentally measured potential *vs.* Ag/AgCl electrode.

To figure out the atomic binding structure and state in the hematite film configuration, X-ray photoelectron spectroscopy (XPS: K-alpha, Thermo UK) has been used to measure the binding energy of the metal ions in the hematite film with a monochromator Al Kα X-ray source. To obtain more specific local binding structural configurations, extended X-ray absorption fine structure (EXAFS) spectra were also obtained using synchrotron radiation in Pohang Accelerator Laboratory (PAL), 1D beam line. Ultraviolet photoelectron spectroscopy (UPS: Thermo Sicentific, ESCALAB 250Xi) was used to figure out the valence band energy levels of hematite thin films.

Results and discussion

One of the specific features of hematite thin films prepared by the DA method is that small hematite particles constituting the hematite thin film cover the surface of the FTO substrate (Fig. 1 and Fig. S1, ESI†).

Different from hematite thin films prepared by other methods such as hydrothermal method, atomic layer deposition method and others, the hematite thin film prepared by the DA method has a very thin hematite layer within about 30 nm on the surface of the FTO substrate. This is clearly shown by the XRD patterns in Fig. 2a. The hematite films prepared by the DA method show some voids as shown by the SEM images in Fig. 1. The dominant XRD peaks of hematite thin films on the FTO surface appeared from FTO. In the XRD patterns of the annealed hematite film at 550 °C (H550), 600 °C (H600), 700 °C (H700) and 800 °C (H800) with 10 DA cycles, the XRD peak intensity from SnO_2 (JCPDS No. 77-0451) is found to be highly dominant compared with pure Fe_2O_3 peaks (JCPDS No. 79-1741) in the case of all types of hematite thin films. It indicates that small hematite particles form an extremely thin film on the surface of the FTO substrate and some of the FTO surface are not fully covered with hematite particles and this makes hematite thin films transparent (Fig. S2, ESI†). To overcome this void area problem, the more compact hematite thin films on the FTO surface were prepared with 20, 30, and 40 DA cycles, additionally. As the number of DA cycles increased, the surface of FTO was completely covered without void area of the FTO substrate as shown in the SEM images (Fig. S3, ESI†). The atomic force microscopy (AFM) images also show that the roughness of the hematite thin film decreased as the number of DA cycles increased and annealing temperature differences (Fig. S4 and S5, ESI†). The root mean square values of surface roughness, R_q, of bare FTO, 10 DA, 20 DA, 30 DA and 40 DA H550 are 44.6 nm, 47.7 nm, 18.1 nm, 10.6 nm and 4.96 nm, respectively.

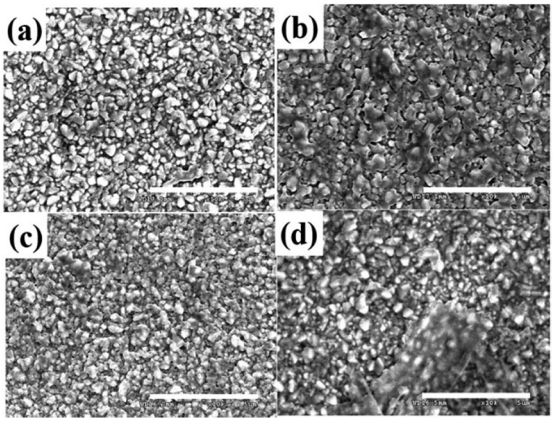

Fig. 1 Top-view SEM images of the 10 DA hematite film (a) H550, (b) H600, (c) H700 and (d) H800 (all scale bars are 5 μm).

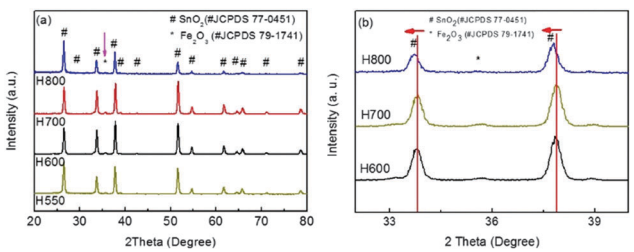

Fig. 2 (a) X-ray diffraction (XRD) patterns of H550, H600, H700 and H800 with 10 DA (b) magnification of XRD patterns from 32° to 41° in 2θ for 10 DA H600, H700 and H800 (SnO_2 for JCPDS No. 77-0451 and α-Fe_2O_3 for JCPDS No. 79-1741).

When 10 DA cycles were performed on the FTO substrate, the roughness value of 10 DA H550 is higher than that of bare FTO due to the voids among the dispersed hematite particles on the surface of bare FTO. Thereafter the number of DA cycle increases from 10 to 40, the roughness values decrease dramatically. That is because the larger numbers of hematite particles fill the voids and cover the surface homogeneously. This is also identified by the XRD patterns of the samples prepared by 20, 30 and 40 DA cycles in Fig. S6 (ESI†). In the XRD patterns, the peak intensity of pure hematite particles gradually increases as the number of DA cycles increases. To find out the relation between the number of DA cycles and photocurrent density, the photocurrent density of each sample prepared with different DA cycles at 550 °C (10 DA, 20 DA, 30 DA, and 40 DA H550) was measured under 1 sun irradiation (Fig. 3a). The 10 DA H550 sample shows the highest photocurrent density.

This result can be explained by comparing the impedance value of each sample at the interface of the hematite–electrolyte solution. In Nyquist plots obtained using electrochemical impedance spectroscopy (Fig. S7, ESI†), the 10 DA H550 sample has the lowest impedance value among the samples prepared with different DA cycles at 550 °C due to the lowest resistivity at the interface. To be focused on the optimum annealing temperature for highest photocurrent density, the samples were prepared with 10 DA cycles at different temperatures.

In Fig. 2b, the XRD patterns show the broad XRD peaks of SnO_2 and the peak position shifts as the annealing temperature increases.

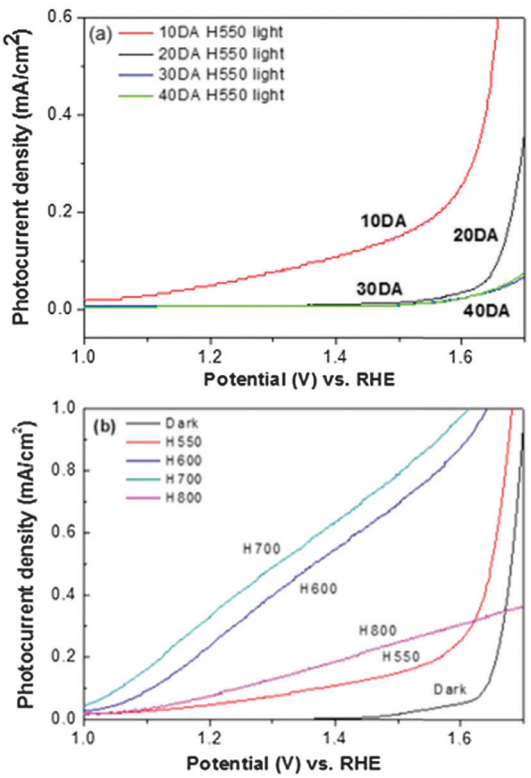

Fig. 3 (a) Photocurrent density curves of H550 with 10 DA, 20 DA, 30 DA, and 40 DA samples. (b) Photocurrent density curves (*I*–*V* curve) of dark, H550, H600, H700 and H800 with 10 DA cycles.

A slight peak shift and decreasing peak intensity of SnO_2 were observed in the case of H800. The peak shift and lower intensity of the SnO_2 XRD patterns can be explained by TEM SAED pattern analysis. H700 shows a clear typical single crystalline SAED pattern without any distortion in the crystal structure of the SnO_2 substrate (Fig. S8a, ESI†). When the annealing temperature reached 800 °C (H800), the crystal structure of the SnO_2 substrate is partially disordered and changed to the amorphous state. This is clearly shown in the SAED pattern of H800 (Fig. S8b, ESI†). The crystal structure of SnO_2 lost its posture to tilt in 66° (from 1 to 1′ position (Fig. S8(b-1) and (b-1′), ESI†), 2 to 2′ position (Fig. S8 (b-2) and (b-2′), ESI†)). The disordered crystalline structure results in a decreasing photocurrent value of the hematite thin film because the disordered crystal structure produces the defects among the hematite films and traps the electron during transportation. This is clearly shown in the highly decreased photocurrent density of hematite thin films annealed at 800 °C (H 800) as shown in Fig. 3(b).

The photocurrent density of the samples prepared with 10 DA cycles at different annealing temperatures (H550, H600, H700 and H800 with 10 DA cycles) has been measured under 1 sun irradiation (Fig. 3b). H700 showed the highest photocurrent density (0.39 mA cm^{-2} at 1.23 V *vs.* RHE, of which potential is water splitting potential). Thereafter, the photocurrent density decreases as the annealing temperature increases and reaches 0.08 mA cm^{-2} at 1.23 V *vs.* RHE for the H800 sample. The photocurrent density of the H700 sample is 8 times enhanced compared with that of H550 (0.05 mA cm^{-2} at 1.23 V *vs.* RHE). To obtain the trend of the photocurrent density value, the hematite films annealed at different temperatures ranging from 550 °C to 600 °C (Fig. S9a, ESI†) and from 700 °C to 800 °C (Fig. S9b, ESI†) were also checked. In Fig. S9b (ESI†), it can be seen that there is a slight onset potential increase as the annealing temperature increases from 700 °C to 800 °C. This is because of the lattice distortion of FTO substrates. The photocurrent density value can be explained with the resistance value of the hematite films measured by electrochemical impedance spectroscopy (EIS) analysis with 1 sun illumination (Fig. 4) and under dark conditions (Fig. S10, ESI†). In Nyquist plots, the impedance value decreased from H550 (14 000 Ohm) to H600 (5000 Ohm) as the annealing temperature increased. The lowest impedance value was obtained with H700 (4000 Ohm). The impedance at the interface of the H800 hematite film–electrolyte solution is determined to be around 11 000 Ohm. This gives a higher energy barrier for the electron flow from the electrolyte solution to the hematite thin film and results in the lower photocurrent density of the hematite film annealed at 800 °C. Also, the starting point of the semicircle for H800 shifted to the higher value. Because of the deformation of the FTO substrate annealed at 800 °C, the overall resistance increased, which was caused by the increase of the resistance of the FTO substrate (Fig. S11, ESI†). To verify whether the photocurrent density value by the change of annealing temperature can be affected by the hematite film or bare FTO substrate, the photocurrent density values of bare FTO substrates annealed at 550 °C (FTO550), 600 °C (FTO600), 700 °C (FTO700), and 800 °C (FTO800) were also measured under 1 sun irradiation

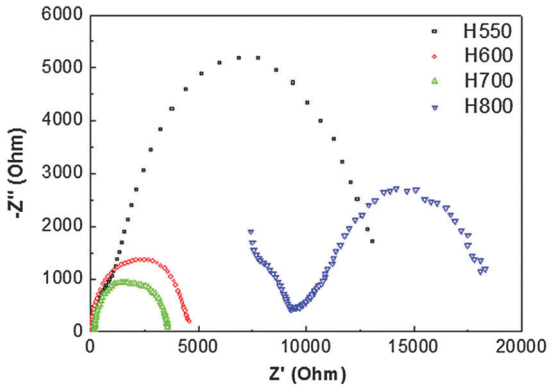

Fig. 4 Nyquist plots of H550, H600, H700 and H800, prepared with 10 DA cycles with 1 sun illumination.

(Fig. S12, ESI†). The photocurrent density of all cases of bare FTO samples is much lower than that of hematite films on FTO substrates regardless of the annealing temperature. This clearly indicates that the effect of the FTO substrate is negligible, considering the photocurrent density of hematite films on FTO substrates.

The partially disordered and aggregated hematite particle structure at the interface between hematite films and FTO substrates was observed in the TEM images of the H700 hematite film (Fig. 5a and b) and the H800 hematite film (Fig. 5c and d). The average distances between hematite particles are 3.5 nm in H700 and 1.27 nm in H800. Especially, in the case of H800, the partially disordered and aggregated structure of hematite particles results in the polycrystalline state. This could provide higher resistance and energy barriers for the electron transport on the surface of hematite film and also the interface junction of the hematite film–FTO substrate by overlapping and aggregating (Fig. 5c, red box). These extremely overlapped and aggregated hematite particles can act as defects for the electron trapping during electron transport. Usually, decreasing inter-lattice distances in single crystal materials enhances electron transportation inside the particle and results in the enhancement of photocurrent density and low impedance values in EIS analysis.[24,25] However, in the case of the polycrystalline or disordered amorphous phase of the hematite film at the interface as shown in TEM images of Fig. 5c and d, even though the particles are close enough to each other, it could result in a higher energy barrier for the electron transport.[26] This can suppress the electron diffusion and cause the enhancement of the electron–hole recombination rate, leading to a decrease of the photocurrent density and an increase of the impedance value of the hematite thin film (Fig. S13, ESI†). Based on this theory, especially in the H800 sample, surface barriers consisted of aggregated hematite particles contributed to increasing surface impedance values of hematite films with a decrease of the photocurrent density value as shown in Fig. 4. The dislocated crystal structure of the SnO_2 substrate also contributed to the decreased photocurrent density. In contrast, decreasing inter-particle distances without any overlapping or aggregation among particles can be attributed to the enhancement of photocurrent density while the annealing temperature increases up to 700 °C, with enhanced electron hopping[27] and long range electron transfer from one particle to another particle[28] with reduced probabilities of electron trapping and electron–hole recombination.

The chemical binding state was also revealed using X-ray photoelectron spectroscopy (XPS) analysis at 25 °C with H600 and H700 samples. The detailed Fe 2p spectra of H600 and H700 are shown in Fig. 6(a). From the peak position and shape of the line, there is no change in the binding state of Fe atoms while the annealing temperature increased from 600 °C to 700 °C. Furthermore, the binding energy values of the Fe $2p_{1/2}$ peak (724.36 eV) and the Fe $2p_{3/2}$ peak (710.96 eV) were also determined as the typical values reported for Fe $2p_{3/2}$ for Fe_2O_3 (Fe^{3+} state, 710.9 eV[29] or 711.2 eV[30]), Fe_3O_4 (Fe^{2+}/Fe^{3+} co-exist state, 709.5 eV[30] for Fe^{2+}, 711.2 eV[30] and 711.6 eV[31] for Fe^{3+}), FeOOH (Fe^{3+} state, 711.2 eV[30] and 711.3–711.9 eV[32]) and these are different from the reported values of FeO (Fe^{2+} state, 709.1–709.5 eV[32] and 709.6 eV[29]). The detailed Sn 3d spectra of H600 and H700 are shown in Fig. 6(b). In the case of H600, the peaks appeared at 495.38 eV for Sn $3d_{3/2}$ and 486.78 eV for Sn $3d_{5/2}$, respectively. These Sn $3d_{3/2}$ and Sn $3d_{5/2}$ peaks are little shifted toward the lower binding energy from typical values of binding energy of Sn $3d_{3/2}$ and Sn $3d_{5/2}$ in the previous report (496.7 eV for Sn $3d_{3/2}$ and 487.9 eV for Sn $3d_{5/2}$)[33] with maintaining the inter-peak distance at 8.7 eV. In the case of H700, the degree of

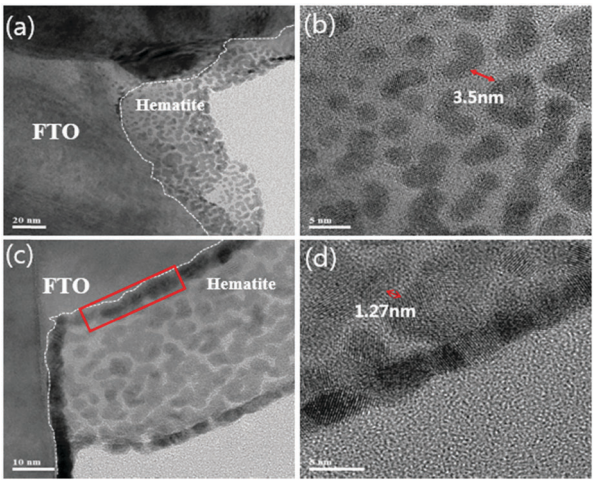

Fig. 5 TEM images of (a) H700, (c) H800 with 10 DA and HR-TEM images (b) H700 and (d) H800 with 10 DA.

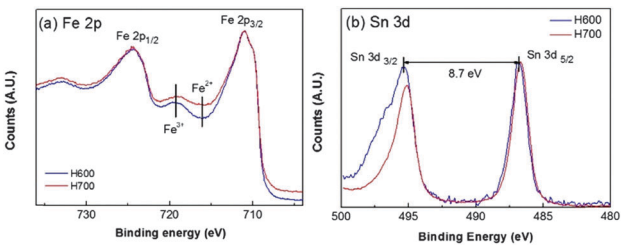

Fig. 6 X-ray photoelectron spectra (XPS) of 10 DA cycles H600 and H700 samples for (a) Fe 2p configuration and (b) Sn 3d configuration.

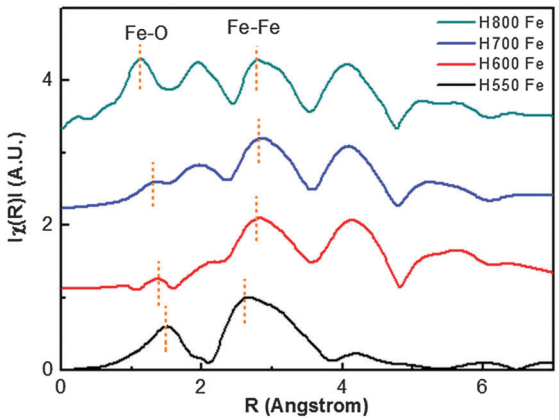

Fig. 7 Extended X-ray absorption fine structure spectrum of the Fe atom in the H550, H600, H700 and H800 with 10 DA cycle samples.

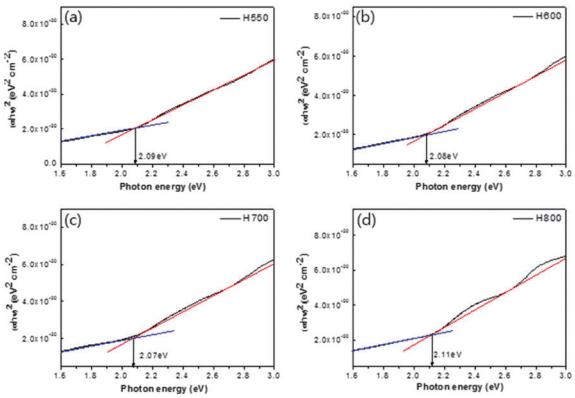

Fig. 8 Tauc plots evaluating the optical band gap are shown for the direct case (a) H550 (b) H600 (c) H700 (d) H800 with 10 DA.

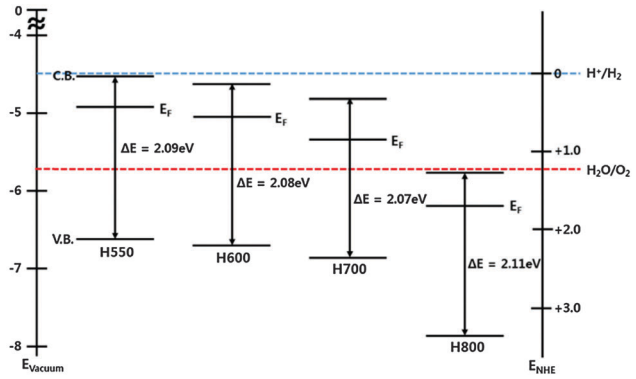

Fig. 9 Schematic drawings of band energies of H550, H600, H700 and H800 with 10 DA cycles, with band gap energy notation.

chemical shift toward a low binding energy increased in Sn $3d_{3/2}$ and Sn $3d_{5/2}$ as 495.15 eV and 486.66 eV, respectively. The chemical shift of Sn 3d toward a lower energy level appeared as the annealing temperature increased in the pure FTO substrate. In Fig. S14(a) (ESI†), Sn $3d_{3/2}$ peaks are found to be shifted from 486.45 eV to 487.03 eV *via* 486.64 eV and Sn $3d_{5/2}$ peaks are shifted from 494.89 eV to 495.51 eV *via* 495.13 eV as the annealing temperature increases from 25 °C to 600 °C *via* 550 °C with maintaining the inter-peak energy difference as 8.42 eV. In the case of O 1s spectra, it is shifted to a higher binding energy state from 530.44 eV to 531.06 eV *via* 530.67 eV as the annealing temperature increases from 25 °C to 600 °C *via* 550 °C (Fig. S14(b), ESI†). The lower binding energy shift of Sn atoms and higher binding energy shift of O atoms with increasing annealing temperature indicate that during the annealing process, fluorine atoms were diffused and disappeared from the FTO substrate and additional oxygen atoms replace fluorine atoms in the same lattice position, forming bonds with Sn atoms. Electron energy loss spectroscopy (EELS) proved that there is no fluorine atom remaining in the FTO substrate when the FTO substrate is annealed at 700 °C for 3 h (Fig. S15, ESI†).

For the detailed local structure, X-ray absorption fine structure (XAFS) analysis has been performed using synchrotron radiation. The extended X-ray absorption fine structure (EXAFS) data were extracted from XAFS data. Extracted EXAFS data were refined and fitted by computational simulations of a typical hematite model in the inorganic crystal structure database[34] with the ifeffit algorithm program as presented in Fig. 7. The iron–oxygen bond length represented in EXAFS was determined to be 1.5 Å in the H550 sample, which is well matched with a previous report.[35] The interatomic distance between the central Fe atom and surrounding oxygen atoms decreased from 1.5 Å of H550 to 1.3 Å of H700. The decreased interatomic distance between Fe and O atoms in the hematite particle might enhance the electron conductivity in the hematite particle due to the short transport distance.

As the band gap value is related to the absorption properties, the optical properties were investigated using UV-vis spectroscopy. To determine the band gap values, Tauc plots[36] of H550, H600, H700 and H800 are drawn in Fig. 8. The band gap energies of each sample are calculated according to the formula as follow;

$$(\alpha\hbar\omega)^{1/m} = B(\hbar\omega - E_g)$$

where α is the optical absorption coefficient, $\hbar\omega$ is the photon energy, E_g is the optical gap energy (eV) and m is an index (m = 1/2 for direct transition and m = 2 for indirect transition). With the slope line of each Tauc plot (red line in Fig. 8), the band gap values were determined to be 2.09 eV for H550, 2.08 eV for H600, 2.07 eV for H700 and 2.11 eV for H800. These band gap energy values roughly match with the band gap of hematite (~2.1 eV) in the previous reports.[11,12] The band gap energy decreases as the annealing temperature increases. This can be explained by the decreasing valence band energy level with increasing annealing temperature, which was measured with UPS spectra as shown in Fig. S16 (ESI†). The schematic band energy diagram based on the valence band energy level and the band gap energy is shown in Fig. 9. This shows the decrease of the band gap and valence band energy.

Conclusion

In summary, the present work reports on the effect of the annealing temperature during the synthesis of hematite thin films on fluorine doped tin oxide substrates by deposition and

annealing method. The hematite films were prepared on FTO substrates in a particle-laying structure and the inter particle distance was decreased as the annealing temperature increases from 550 °C (H550) to 800 °C (H800). As the annealing temperature increases, the hematite thin film showed the highest photoelectro-chemical properties at 700 °C (H700) and thereafter the photoelectrochemical efficiency was decreased at 800 °C (H800). This is due to the distortion of the crystal structure in the FTO substrate and the increased resistance of the hematite film surface by the aggregated polycrystalline hematite particles. Thus, this work reported the optimal annealing temperature of the hematite thin film on a FTO substrate by facile methods for synthesizing hematite films. However, strategies to overcome the lower photocurrent density of hematite film synthesized by the DA method compared to other synthesizing methods[37–39] should be studied more.

Notes and references

1 M. Grätzel, *Nature*, 2001, **414**, 338–344.
2 A. Kay, I. Cesar and M. Grätzel, *J. Am. Chem. Soc.*, 2006, **128**, 15714–15721.
3 G. Wang, X. Yang, F. Qian, J. Z. Zhang and Y. Li, *Nano Lett.*, 2010, **10**, 1088–1092.
4 R. Liu, Y. Lin, L. Chou, S. W. Sheehan, W. He, F. Zhang, H. J. M. Hou and D. Wang, *Angew. Chem., Int. Ed.*, 2011, **50**, 499–502.
5 X. Y. Yang, A. Wolcott, G. Wang, A. Sobo, R. C. Fitzmorris, F. Qian, J. Z. Zhang and Y. Li, *Nano Lett.*, 2009, **9**, 2331–2336.
6 J. Hensel, G. Wang, Y. Li and J. Z. Zhang, *Nano Lett.*, 2010, **10**, 478–483.
7 R. Solarska, A. Krolikowska and J. Augustyński, *Angew. Chem., Int. Ed.*, 2010, **49**, 7980–7983.
8 J. Su, X. Feng, J. D. Sloppy, L. Guo and C. A. Grimes, *Nano Lett.*, 2011, **11**, 203–208.
9 S. D. Tilley, M. Cornuz, K. Sivula and M. Grätzel, *Angew. Chem., Int. Ed.*, 2010, **49**, 6405–6408.
10 F. Qian, G. Wang and Y. Li, *Nano Lett.*, 2010, **10**, 4686–4691.
11 A. Duret and M. Grätzel, *J. Phys. Chem. B*, 2005, **109**, 17184–17191.
12 A. B. Murphy, P. R. F. Barnes, L. K. Randeniya, I. C. Plumb, I. E. Grey, M. D. Horne and J. A. Glasscock, *Int. J. Hydrogen Energy*, 2006, **31**, 1999–2017.
13 O. Khaselev and J. A. Turner, *Science*, 1998, **280**, 425–427.
14 Y. Ling, G. Wang, D. A. Wheeler, J. Z. Zhang and Y. Li, *Nano Lett.*, 2011, **11**, 2119–2125.
15 H. G. Cha, J. Song, H. S. Kim, W. Shin, K. B. Yoon and Y. S. Kang, *Chem. Commun.*, 2010, **47**, 2441–2443.
16 N. J. Cherepy, D. B. Liston, J. A. Lovejoy, H. Deng and J. Z. Zhang, *J. Phys. Chem. B*, 1998, **102**, 770–776.
17 Y. Lin, Y. Xu, M. T. Mayer, Z. I. Simpson, G. McMahon, S. Zhou and D. Wang, *J. Am. Chem. Soc.*, 2012, **134**, 5508–5511.
18 Y. Lin, S. Zhou, S. W. Sheehan and D. Wang, *J. Am. Chem. Soc.*, 2011, **133**, 2398–2401.
19 B. M. Klahr, A. B. F. Martinson and T. W. Hamann, *Langmuir*, 2011, **27**, 461–468.
20 D. K. Zhong, M. Cornuz, K. Sivula, M. Grätzel and D. R. Gamelin, *Energy Environ. Sci.*, 2011, **4**, 1759–1764.
21 I. Cesar, A. Kay, J. A. G. Martinez and M. Grätzel, *J. Am. Chem. Soc.*, 2006, **128**, 4582–4583.
22 G. Wang, Y. Ling, D. A. Wheeler, K. E. N. George, K. Horsley, C. Heske, J. Z. Zhang and Y. Li, *Nano Lett.*, 2011, **11**, 3503–3509.
23 J. H. Kennedy and K. W. Frese, *J. Electrochem. Soc.*, 1978, **125**, 723–726.
24 N. Tessler, Y. Preezant, N. Rappaport and Y. Roichman, *Adv. Mater.*, 2009, **21**, 2741.
25 M. Y. Han, J. C. Brant and P. Kim, *Phys. Rev. Lett.*, 2010, **104**, 056801.
26 E. A. Davis and N. F. Mott, *Philos. Mag.*, 1970, **179**, 903–922.
27 Z. Shuai, L. Wang and C. Song, *Theory of Charge Transport in Carbon Electronic Materials*, SpringerBriefs in Molecular Science, Springer, 2012, pp. 7–40.
28 B. Juan, *Phys. Chem. Chem. Phys.*, 2008, **10**, 3175–3194.
29 D. Briggs and M. P. Seah, *Practical Surface Analysis, Auger and X-ray Photoelectron Spectroscopy*, Wiley, New York, 1990, vol. 1, Appendix 1.
30 K. Wandelt, *Surf. Sci. Rep.*, 1982, **2**, 1–121.
31 P. Mills and J. L. Sullivan, *J. Phys. D: Appl. Phys.*, 1983, **16**, 723–732.
32 J. F. Moulder, W. F. Stickle, P. E. Sobol and K. D. Bomben, *Handbook of X-ray Photoelectron Spectroscopy*, Physical Electronics, Eden Prairie, 1995.
33 B. V. Crist, *Handbook of Monochromatic XPS spectra: Semiconductors*, John Wiley & Sons Ltd, England, 2000, pp. 501–506.
34 L. Pauling and S. B. Hendricks, *J. Am. Chem. Soc.*, 1925, **47**, 781–790.
35 G. Gilbert, C. Frandsen, E. R. Maxey and D. M. Sherman, *Phys. Rev.*, 2009, **79**, 035108.
36 J. Tauc, R. Grigorov and A. Vancu, *Phys. Status Solidi*, 1966, **15**, 627–637.
37 J. Brillet, M. Grätzel and K. Sivula, *Nano Lett.*, 2010, **10**, 4155–4160.
38 R. H. Goncalves, B. H. R. Lima and E. R. Leite, *J. Am. Chem. Soc.*, 2011, **133**, 6012–6019.
39 C. X. Kronawitter, I. Zegkinoglou, C. Rogero, S. S. Mao, F. J. Himpsel and L. Vayssieres, *J. Phys. Chem. C*, 2012, **116**, 22780–22785.

